nature materials

SUPPLEMENTARY INFORMATION

DOI: 10.1038/NMAT4719

The nanocomposite nature of bone drives its strength and damage resistance

Ottman A. Tertuliano, Julia R. Greer

1. Crystallization of ACP with time

To probe the stability of the observed ACP in disordered phase with respect to the adjacent HA nanocrystals, we performed TEM analysis of the same region after a 30-day time lapse. During the 30 days, the TEM sample was stored at room temperature in a N_2 environment. Figure S1a shows the initial arrangement of ACP (left) and HA nanocrystals (right), as well as the diffraction pattern inset showing the crystallinity of the HA. Figure S1b shows the same region after the 30 day incubation period; the HA nanocrystals on the right appear to have grown, confirmed by the increased (112), (211), (300) intensities in the diffraction pattern inset; we also observe the emergence of (002) reflections after one month, which further proves the formation of crystals. These results demonstrate suggest that biogenic ACP is a precursor for crystalline cHA formation in bone in the observed conditions, as similarly observed by Mahamid et al[1].

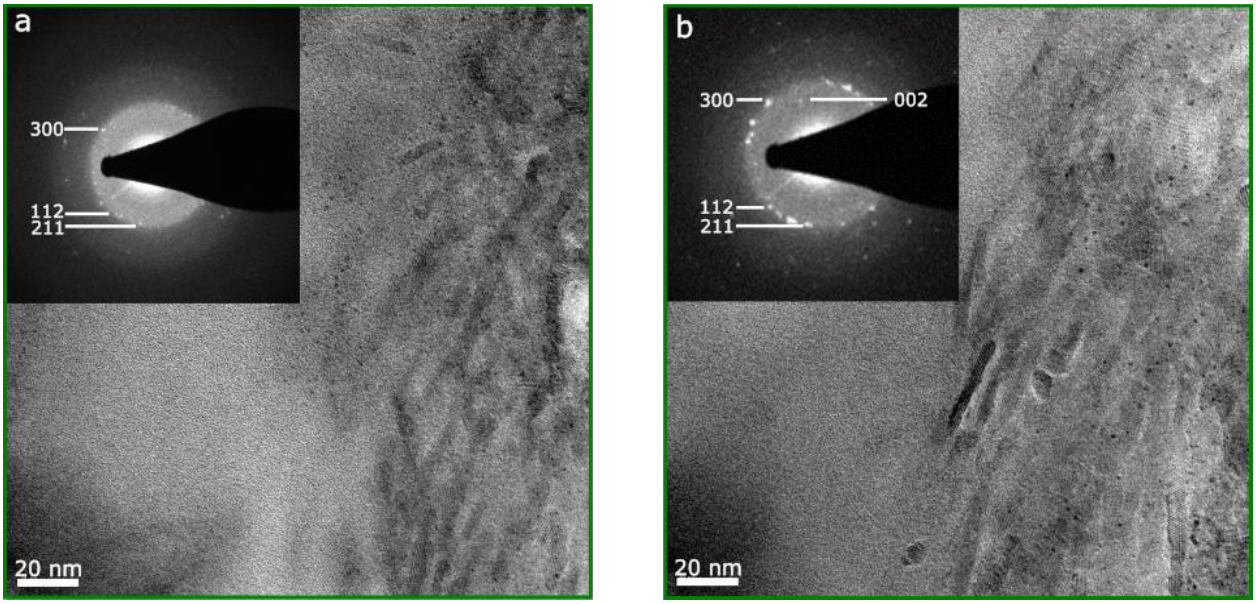

Figure S1. Time lapse micrographs of amorphous and nanocrystalline regions. Deprotonated mineral structure in disordered phase taken before (a) and after (b) a 30 day incubation at room temperature in a nitrogen environment. The electron diffraction pattern after the incubation (b, inset) shows an increase in crystallinity as evidenced by more intense HA reflections and the emergence of the (002) spots when compared to the initial diffraction pattern (a, inset).

2. Size Dependent Model Construction

We propose that the yield strength, σ_{yield} , decreases as the probability of having a flaw (i.e. a pore) on the pillar surface increases; that is, surface flaws serve as probabilistic stress concentrators, which initiate failure during compression. This is manifested most prevalently in the larger pillars, with diameters > 500nm. At these nano and micro length scales, it is reasonable to consider bone as a fiber-

reinforced composite; hence we should also consider microstructural stress concentrations, i.e. ones that arise from stiff fiber reinforcements in a more compliant matrix. To quantify these effects and to capture their effect on the observed size dependent strength, we calculate the stress concentrations for two different representations of bone: 1) we model the ordered and disordered phases as fiber-reinforced composites to evaluate the stress concentrations that arise from stiff fibers and 2) we consider the small-scale samples as a homogenous continuum medium with randomly distributed pores to evaluate the stress concentrations caused by surface flaws, i.e. pores. We then compare the stress concentrations from each of these components and employ the strongest stress concentrator to quantitatively describe the emergent size effects in ordered and disordered phases of bone.

2. 1 Stress concentration from fibers

The stress concentration factor that arises from the stiff fiber reinforcements in a composite, k_f, can be represented as

$$k_f = \frac{1 - \phi_f \left(\frac{E_m}{E_f}\right)}{1 - \left(\frac{\phi_f}{\phi_{fmax}}\right)^{\frac{1}{2}} \left(\frac{E_m}{E_f}\right)} \quad (1)$$

where ϕ_f is the volume fraction of the fibers, ϕ_{fmax} is the close-packing fraction of the fibers based on the assumed packing configuration of the fibers (i.e hexagonal, square, random), and E_m and E_f are the matrix and fiber elastic moduli, respectively[2]. Eq. 1 is only valid for the cases when the fibers are stiffer than the matrix. To employ this principle, we must first define the functional fibril and matrix in the bone composite. The gap and the overlapping regions within the collagen fibril structure, shown and labeled in Figure S2 have been reported to contain some mineral[3,4] , which gives rise to a mineralized fibril, for which we use the subscript "MF" in our model construction. The mineral external to the fibril can be either tightly bound to the surface of the MF[5], which gives rise to a coated mineralized fibril, here referred to as CMF, or be a part of the extrafibrillar matrix, which we refer to as "EFM". The CMFs have been experimentally observed in bone, bridging cracks in [6] and on failure surfaces[7], which suggests that it is important and relevant to calculate the stress concentration due to CMFs, k_{CMF}.

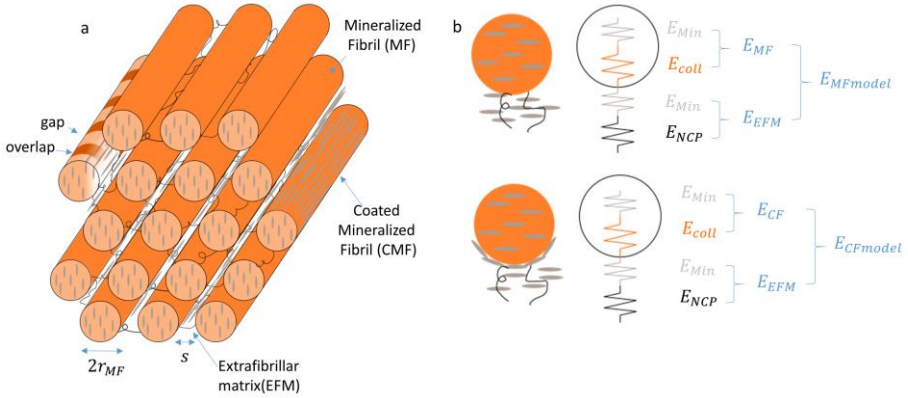

Figure S2. a) Hexagonally arranged ordered fibrils with MF radii r_{MF} and some spacing s. B) Schematics of the MF and CMF models showing a Reuss, or series, model of the stiffness contributions from the mineral, collagen, and NCPs.

We have not been able to find any literature that reports the elastic properties or volume fractions of CMFs or the complementary EFM; this is likely due to the difficulty of isolating these constituents in experiments and the lack of consensus on the spatial distribution of bone mineral in models and computational efforts. The exact spatial distribution of mineral (intrafibrillar vs extrafibrillar) in bone is still under debate in the literature, ranging from 30% to 75% of the total mineral being extrafibrillar[8,9], and the amount of extrafibrillar mineral bound to the surface of the fibril has received little attention[10]. Most elastic models of bone at these nano- and micro- length scales do not take into consideration extrafibrillar mineralization[3,11] and those that do assume some initial extrafibrillar vs intrafibrillar mineral distribution[10,12]. Understanding the spatial distributions of bone constituents at these length scales is necessary for calculating k_{CMF}. We calculate k_{CMF} without assuming an initial mineral distribution by modelling bone as a fiber-reinforced composite in two stages: 1) a *MF model* with MFs contained in an EFM, composed of non-collagenous proteins(NCPs), mineral, and pores, and 2) a *CMF model,* in which some mineral from the MF's model EFM is bound to the surface of the CMF, i.e the MF is grown into a stiffer CMF by absorbing mineral from the EFM. These two models are illustrated in Figure S2.

We use the MF model to determine the volume fractions of each fundamental constituent, i.e. collagen, mineral, and non-collagenous proteins(NCPs), as well as the extrafibrilar vs intrafibrillar distribution the mineral. We accomplish this by using the elastic moduli measured in our experiments as constraints for the eigenstress (Ruess) elastic model of the composite. Next, we re-allocate the mineral from the EFM to the MF to "create" a stiff CMF in a more compliant EFM, which allows us to calculate k_{CMF}.

2.1.1 MF model

The ordered phase composite is depicted as hexagonally arranged fibrils in the EFM, similar to the arrangement assumed by Nikolov and Raabe (ref 10 and Fig. S2a). Then, the elastic modulus of the overall composite in terms of the elastic properties of the MF and the EFM is

$$E_{MFmodel} = \left(\frac{\phi_{MF}}{E_{MF}} + \frac{1-\phi_{MF}}{E_{EFM}}\right)^{-1} \tag{2}$$

where

$$E_{MF} = \left(\frac{\phi_{Min}^{MF}}{E_{Min}} + \frac{1-\phi_{Min}^{MF}}{E_{Coll}}\right)^{-1} \tag{3}$$

and

$$E_{EFM} = \left(1-\phi_{pores}^{EFM}\right)\left(\frac{\phi_{Min}^{EFM}}{E_{Min}} + \frac{1-\phi_{Min}^{EFM}}{E_{NCP}}\right)^{-1} \tag{4}$$

E_{coll}, E_{Min}, and E_{NCP} are the elastic moduli of the collagen, mineral, and non-collagenous proteins, respectively.

To account for the porosity in the composite models, we assume that all pores are located in the extrafibrillar space as opposed to within the fibers; the prefactor in Eq.4 accounts for a reduction of E_{EFM} caused by the volume fraction of pores in the EFM, ϕ_{pores}^{EFM}. This fraction can be determined from

the total pore volume fraction, ϕ_{pores}, measured in our experiments and shown in Supplementary Videos 1&2.

$$\phi_{pores}^{EFM} = \frac{\phi_{pores}}{\phi_{EFM}} \tag{5}$$

To calculate ϕ_{EFM}, we note that in a hexagonal array of fibers, the relative fraction of the matrix as a function of the spacing between the fibers, s , is given by

$$\phi_{EFM} = 1 - \phi_{MF} \tag{6a}$$

$$\phi_{EFM}[s] = 1 - \frac{2\pi r_{MF}^2}{3^{\frac{1}{2}}(2r_{MF} + s)^2} \tag{6b}$$

where ϕ_{MF} is the volume fraction of MFs. The average radius of the pores is some linear fraction, x, of the spacing between fibrils, so we can relate s and x through:

$$s[x] = (x)2r_{pores} + (1 - x)s_{solid} \tag{7}$$

$$x[s] = \frac{s - s_{solid}}{2r_{pores} + s_{solid}} \tag{8}$$

Here, s_{solid} is the extrafibrillar linear spacing if no pores were present; we assume s_{solid} to be ~12 nm based on Nikolov and Raabe [10], and r_{pores} is 20.8nm, measured in this work for the ordered phase. It is reasonable to assume that the linear fraction of the pores can be related to their volume fraction in the EFM through $x^3 \sim \phi_{flaw}^{EFM}$, which allows us to calculate $s = 36.5\ nm$, $\phi_{EFM}^{ord} = 0.51$ and $\phi_{flaw}^{EFM} = 0.096$ for the ordered phase.

For the disordered phase, the hexagonal geometrical argument is not applicable, but by constraining the pores to the EFM, we can assume that ϕ_{EFM} scales with ϕ_{pores} ; that is ϕ_{pores}^{EFM} is constant across both phases. To calculate the fraction of EFM in the disordered phase, ϕ_{EFM}^{disor}, we scale ϕ_{EFM}^{ord} by the ratio of pore volume fractions in the two phases (Eq.9), resulting in $\phi_{EFM}^{disor} = 0.63$.

$$\phi_{EFM}^{disord} = \frac{\phi_{pores}^{disord}}{\phi_{poree}^{ord}} \phi_{EFM}^{ord} \tag{9}$$

Next, we can resolve the remaining volume fractions in Eqs. (2)-(4) in terms of the fraction of total mineral that is extrafibrillar, as ϕ_{EF}^{Min} . In this context, the fraction of the mineral that is intrafibrillar is

$$\phi_{IF}^{Min} = 1 - \phi_{EF}^{Min} \tag{10}$$

To determine the total mineral volume fraction, ϕ_{Min} , we define the total intrafibrillar mineral fraction, ϕ_{MinIF} in two ways:

$$\phi_{MinIF} = \phi_{MF}\phi_{Min}^{MF} \tag{11a}$$

and

$$\phi_{MinIF} = \phi_{Min}\phi_{IF}^{Min} \tag{11b}$$

where ϕ_{Min}^{MF} is the fraction of the MF that is mineral and ϕ_{IF}^{Min} is the fraction of the total mineral that is intrafibrillar (note ϕ_{MinIF} and ϕ_{IF}^{Min} are not equivalent). Equating Eqs. (11a) and (11b), we get

$$\phi_{Min} = \frac{\phi_{MF}\phi_{Min}^{MF}}{\phi_{IF}^{Min}} \tag{11c}$$

Using similar relations for the EFM, we can solve for the fraction of EFM that is mineral, ϕ_{Min}^{EFM}:

$$\phi_{MinEF} = \phi_{EFM}\phi_{Min}^{EFM} \tag{12a}$$

$$\phi_{MinEF} = \phi_{Min}\phi_{EF}^{Min} \tag{12b}$$

$$\phi_{Min}^{EFM} = \frac{\phi_{Min}\phi_{EF}^{Min}}{\phi_{EFM}} \tag{12c}$$

With this series of relations dependent inherently on ϕ_{EF}^{Min}, all variables that define $E_{MFmodel}$ can be solved for. The main assumed parameter in the MF model is the fraction of the MF that is mineral, that is the amount of mineral that a MF can internally accommodate. We assume this to be ~0.42 as analytically calculated by Jäger and Fratzl (3) and corroborated by Nair et al**.(**11**)** via molecular dynamics simulations. We tabulate the elastic properties of the fundamental constituents, E_{coll} , E_{Min}, and E_{NCP}, as well as other assumed parameters, used in the calculations presented here in Table 1. We account for the anisotropy in the elastic contributions of collagen and mineral by using the transverse orientation values of E_{coll} and E_{Min} , respectively, for the ordered phase. For the disordered phase we use the mean values of the transverse and axial E_{coll} and E_{Min} .

Using *Mathematica*, the system of Eqs. (2)-(4) and (10)-(12) is solved for both the ordered and disordered phase by setting $E_{MFmodel}$ equal to their respective mean elastic moduli as measured in this work via nanoindentation, 16.3 GPa for ordered, and 21.0 GPa for disordered. It is important to note that the Ruess model formulation above accounts for porosity by effectively reducing the E_{Min} and E_{NCP} contributions to E_{EFM}(Eq. 4) but the flaw volume fraction is initially not an inherent part of ϕ_{EFM} . We account for this by adjusting the volume fractions, as shown in Appendix 1. The final resulting volume fractions and distributions are reported in Table 2 for both phases. We calculate that ~68.8% of the mineral is extrafibrillar in the ordered phase and 77.9% in the disordered phase. This falls in line with the literature that suggests most the mineral is located outside the fibril[9,13]. Although this model only considered dry bone, it is noteworthy that the ϕ_{EF}^{Min} is just the percentage of total mineral fraction ϕ_{Min} that is outside the fibril and thus could remain constant even if ϕ_{Min} decreased once water is introduced.

Table S1. List of parameters used in the MF and CMF models

Parameter	Description	Value	Reference
ϕ_{Min}^{MF}	fraction of MF that is mineral	.42	Jäger & Fratzl 2000
ϕ_{Col}^{MF}	fraction of MF that is collagen	.58	Jäger & Fratzl 2000
ϕ_{pores}	fraction of bone phase that is porous {ord, disord}	{.49,.59}	present study
$r_{MF}[nm]$	radius of MF	50	Hassenkam et al. 2004
$r_{flaws}[nm]$	average radius of flaws {ord, disord}	{20.08 , 18.6}	present study
$s_{solid}[nm]$	Non-porous linear spacing between hexagonally arranged MF		Nikolv & Raabe 2008
$E_{Min}[GPa]$	elastic modulus of mineral {transverse, axial}	{100 , 128}	{Nikolov& Raabe 2008, Viswanath et al. 2007}
$E_{Coll}[GPa]$	elastic modulus of dry collagen {transverse, axial}	{7.5 , 10.65}	{Wenger et al. 2007, Cusack & Miller 1979}
$E_{NCP}[GPa]$	elastic modulus of non-collagenous proteins	1	Nikolov & Raabe 2008
$E_{ord}[GPa]$	elastic modulus of ordered phase	16.3	present study
$E_{disord}[GPa]$	elastic modulus of disordered phase	21.0	present study

Table S2. Results of MF and CMF models

Variable	Description	Result	
		Ordered	Disordered
ϕ_{Min}	fraction of tissue that is mineral	0.655	0.710
ϕ_{Col}	collagen volume fraction	0.282	0.217
ϕ_{NCP}	non-collagenous proteins volume fraction	0.013	0.013
ϕ_{MF}	mineralized fibril volume fraction	0.486	.374
ϕ_{CMF}	coated mineralized fibril volume fraction	0.794	.640
ϕ_{EFM}	extrafibrillar matrix volume fraction {MF, CMF}	{0.514 , 0.206}	{0.626 , 0.360}
ϕ_{EF}^{Min}	fraction of mineral that is extrafibrillar	0.688	0.779
ϕ_{IF}^{Min}	fraction of mineral that is intrafibrillar	0.312	0.221
ϕ_{Min}^{EFM}	fraction of EFM that is mineral {MF, CMF}	{0.878 , 0.840}	{0.883 , 0.866}
ϕ_{NCP}^{EFM}	fraction of EFM that is NCP {MF, CMF}	{0.026 , 0.064}	{0.021 , 0.038}
ϕ_{Pores}^{EFM}	fraction of EFM that is pores	0.096	0.096
k_{CMF}	stress concentration factor	1.09	1.08

2.1.2 Stress concentration from fibers: CMF model

We formulate the CMF model by increasing the volume fraction of the mineral in the MF, by adding the contribution of the mineral from the EFM, reallocated to the surface of the formed CMF (Fig S2). This results in increasing the stiffness of the fibril with respect to the EFM; because the volume fractions of the fundamental constituents are constant from the MF to the CMF model, the two model are equivalent in terms of the elastic properties of the composite, $E_{MFmodel} = E_{CMFmodel}$. Similar to the MF model, we define the elastic modulus of the CMF as

$$E_{CMFmodel} = \left(\frac{\phi_{CMF}}{E_{CMF}} + \frac{1-\phi_{CMF}}{E_{EFM}}\right)^{-1} \tag{13}$$

where the elastic modulus of the CMF unit and EFM, E_{CF} and E_{EFM} are represented as

$$E_{CMF} = \left(\frac{\phi_{Col}^{CMF}}{E_{Col\_Dry}} + \frac{\phi_{MinIF}^{CMF}}{E_{Min}} + \frac{1-\phi_{Col}^{CMF}-\phi_{MinIF}^{CMF}}{E_{Min}(1-\phi_{flaws}^{EFM})}\right)^{-1} \tag{14}$$

and

$$E_{EFM} = \left(1-\phi_{flaws}^{EFM}\right)\left(\frac{\phi_{Min}^{EFM}}{E_{Min}} + \frac{1-\phi_{Min}^{EFM}}{E_{NCP}}\right)^{-1} \tag{15}$$

The first and second terms in Eq.14 are the fractions of the CMF that are collagen and internal mineral, respectively, defined as

$$\phi_{Coll}^{CMF} = \phi_{Coll}^{MF}\left(\frac{\phi_{MF}}{\phi_{CMF}}\right) \tag{16}$$

and

$$\phi_{MinIF}^{CMF} = \phi_{Min}^{MF}\left(\frac{\phi_{MF}}{\phi_{CMF}}\right) \tag{17}$$

The third term in Eq.14 reflects the contribution of the mineral on the external surface of the fibril to the CMF stiffness, accounting for porosity in the EMF as explained in detail in the MF model section.

The remaining mineral in the tissue composes a fraction of the EFM, ϕ_{Min}^{EFM}; defined as

$$\phi_{Min}^{EFM} = \frac{\phi_{Min} - \left(1-\phi_{Coll}^{CMF}\right)\phi_{CMF}}{1-\phi_{CMF}} \tag{18}$$

where the term $\left(1-\phi_{Coll}^{CMF}\right)\phi_{CMF}$ is the fraction of tissue that is mineral and part of the CMF, with $1-\phi_{CMF} = \phi_{EFM}$.

In a similar fashion to the MF model, the unknown fractions can be solved for in terms of one unknown, in this case ϕ_{CMF} ., To determine ϕ_{CMF} that yields a CMF that is stiffer than the EFM and calculate a valid stress concentration factor due to CMFs , in Figures S3 and we plot E_{CMF} , E_{EFM}, and $E_{Ordered}$ (Fig S3a)or $E_{Disordered}$ (Fig S3a)as functions of ϕ_{CMF} for $\phi_{MF} \leq \phi_{CMF} \leq \phi_{fmax}$, that is from the no reallocated mineral fraction of CMFs to fiber close-packing fraction CMFs. We also plot k_{CMF}, the stress

concentration caused by CMFs as a function of ϕ_{CMF}. In the context of this model, the physical lower bound for ϕ_{CMF} is the fraction at which E_{CMF} and E_{EFM} are equal and the upper bound is the close-packing fraction of the fibers; this range is shaded and labeled as the k_{CMF}-valid region in Figure S3. For both ordered and disordered phases, k_{CMF} only deviates from linearity with respect to ϕ_{CMF} near the upper bound of the region; we take the average ϕ_{CMF} in this region and calculate k_{CMF} to be 1.09 for the ordered phase and 1.08 for the disordered. We now compare this value to the stress concentration that arises from the surface pores calculated in the next section.

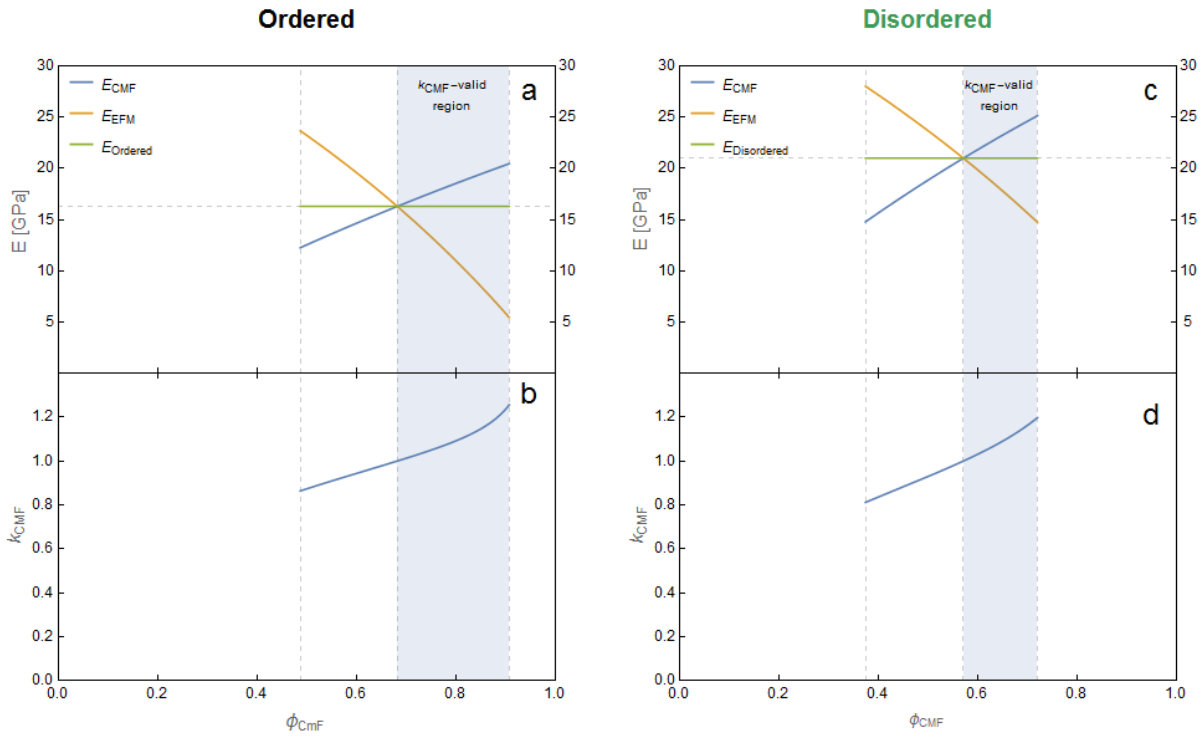

Figure S3. a,c) Show the elastic modulus of the CMF, EFM, and corresponding, composite ordered (a) or disordered (c). The composite moduli are constant because an increase in ϕ_{CMF} corresponds to r mineral form the EFM to the CMF, thus the overall composite properties do not change. The plots are shown from with the lower bound of ϕ_{CMF} corresponding to ϕ_{MF} and the upper bound corresponding to the close packing of the fiber, 0.9069 for hexagonally close packed and ~0.72 for disordered fibers[14] . b,d) Show the stress concentration k_{CMF} due to the CMF. The shaded region, showing where k_{CMF} is valid, has a lower bound at the fraction at which E_{CMF} and E_{EFM} are equal and an upper bound at the close packing fraction.

2.2 Stress concentration from flaws

We can define the stress concentrations that arise from the internal flaws as $k_{internal}$ and those from surface flaws as $k_{surface}$. If we assume the flaws to circular pores in an isotropic continuum, we can approximate $k_{internal}$ as the stress concentration due to the internal spherical voids in a continuum body given by Timoshenko and Goodier[15] as

$$k_{internal} = \frac{27 - 15\,\nu}{2(7 - 5\,\nu)} \tag{19}$$

where ν is the Poisson's ratio. Taking $\nu = 0.3$ for bone[16], we calculate $k_{internal} to\ be\ 2.05$. With a similar assumption of circular pores in an isotropic continuum, we can approximate an upper bound for $k_{surface}$ as the stress concentration of a hole on the side of a thin plate, given by Inglis[17] as

$$k_{surface} = 1 + 2\frac{a}{b} \tag{22}$$

where a and b are the major and the minor axes of an ellipse, in our case set as equal; we calculate $k_{surface} = 3.00$

2.3 Comparison of stress concentrators

We calculated the stress concentrations that arise from each relevant contribution in small-scale trabecular bone samples: the stiff fiber reinforcements in ordered and disordered phases, $k_{CMF} = 1.09$ and 1.08, respectively, the internal flaws $k_{internal} = 2.05$, and the surface flaws, $k_{surface} = 3.00$ for both phases. This shows that the strongest stress concentrators in the system are the surface flaws, or pores, consistent with the experimental observations. This result gives us a starting point to justify the hypothesis that serves as the underlying mechanism for failure initiation occurring at the surface flaws in small-scale bone samples. We postulate in the main body of this manuscript that the surface flaws serve as probabilistic stress concentrators and determine the yield stress, or initiation of failure, of the sample.

2.4 Effective stress concentration from surface flaws

In the spirit of a stochastic dislocations source length model constructed by Parthasarathy[18] to predict a "smaller is stronger" size effect observed in polycrystalline metallic pillars, we conceive a 2D model of a cross-section of radius R and of unit thickness. The cross section is orthogonal the pillar axis (Fig. 4b in the main manuscript). We define n flaws, all of which we simplify to circles of mean radii r. The i^{th} flaw is a distance d_i from the surface of the pillar of radius R. There is a surface flaw if the minimum of the set distances, d_i, is less than or equal to r (Eq. 23). Equivalently, a surface flaw exists if a flaw is at a distance $d_i \leq r$ from the boundary of the cross-section. We also define the cumulative distribution function (CDF) of d_i in Eq. 24 , stating the density of flaws at some distance r drops of with the square of that distance from the surface.

$$min\{d_1, \dots, d_n\} \leq r \tag{23}$$

$$F_{d_i} = 1 - \left(1 - \frac{r}{R}\right)^2 \tag{24}$$

We construct Eqs. 25-31 to reflect our hypothesis. In Eq. 25, we define the relation for yield strength, σ_{yield} , as a product of the bulk strength and an effective stress concentration factor, σ_{bulk} and k_{eff} , respectively.

$$\sigma_{yield} = \sigma_{bulk} k_{eff} \tag{25}$$

For each phase, ordered and disordered, we take the bulk strength to be the strength of the 3µm pillars. We propose that k_{eff} increases with the probability that a surface flaw exists, denoted as P_s in Eq. 26.

$$k_{eff} = P_s + (1 - P_s) k_{surface} \tag{26}$$

The upper bound for k_{eff} is $k_{surface} = 3$, as calculated in the previous section.

We substitute Eq. 26 into 25, stating a pillar becomes stronger as the probability of stress concentration due to surface flaws decreases:

$$\sigma_{yield} = \sigma_{bulk}(P_s + (1 - P_s) k_{surface}) \tag{27}$$

We can define the probability, P_s , using the pillar radius by assuming the volume fraction of flaws across the range of pillars is constant. This assumption is reasonable in each phase because the pillars are fabricated in the sub-lamella length scale, meaning the microstructure should be consistent since lamella interfaces are not present. Keeping in mind the 2D simplification of unit thickness (a thin cross-sectional slice), we define P_s as the probability that the minimum of the distances of the n flaws in the cross-section is less than or equal to r.

$$\begin{aligned} P_s &= P\left[d_{i_{min}} \leq r\right] = P[min\{d_1, \dots, d_n\} \leq r] \\ &= 1 - P[\{d_1, \dots, d_n\} > r] \\ &= 1 - (1 - P[d_i \leq r]^n) \\ &= 1 - \left(1 - F_{d_i}[r]\right)^n \\ &= 1 - \left(\left(1 - \frac{r}{R}\right)^2\right)^n \end{aligned} \tag{28}$$

Eq. 29 shows the number of flaws, n, scales with R^2, assuming the volume faction of flaws, ϕ, is constant.

$$n = \phi \left(\frac{R}{r}\right)^2 \tag{29}$$

To expand the unit thickness cross-section model to a 3D, we can assuming we have l independent slices of unit thickness; this is results in nl rather and n flaws for the number of flaws in the full pillar. The corrected probability P_s is shown in Eq. 30.

$$P_s = 1 - \left(\left(1 - \frac{r}{R}\right)^2\right)^{nl} \tag{30}$$

The pillars are fabricated to have aspect ratios of 3:1, length to diameter; thus l is approximately equal to $6R$. We can now summarize the yield strength as a function of pillar radius:

$$\sigma_{yield}[r] = \sigma_{bulk}\left(1 - 2\left(\left(1 - \frac{r}{R}\right)^2\right)^{6\phi\frac{R^3}{r^2}}\right) \quad (31)$$

In Matlab, we use image contrast thresholding to identify and quantify the porosity across 42 cross-sections in each phase, ordered and disordered. We calculate and measure ϕ to be 0.493 for the ordered phase and 0.590 for the disordered phase and r to be 20.8 ± 11.0 nm for the ordered phase and r = 18.1 ± 9.4 nm for the disordered phase. Videos of the cross-sections used for measuring ϕ and r within the ordered and disordered phases are provided in Supplemental Videos 1 and 2 and the Matlab script is available in Appendix 2.

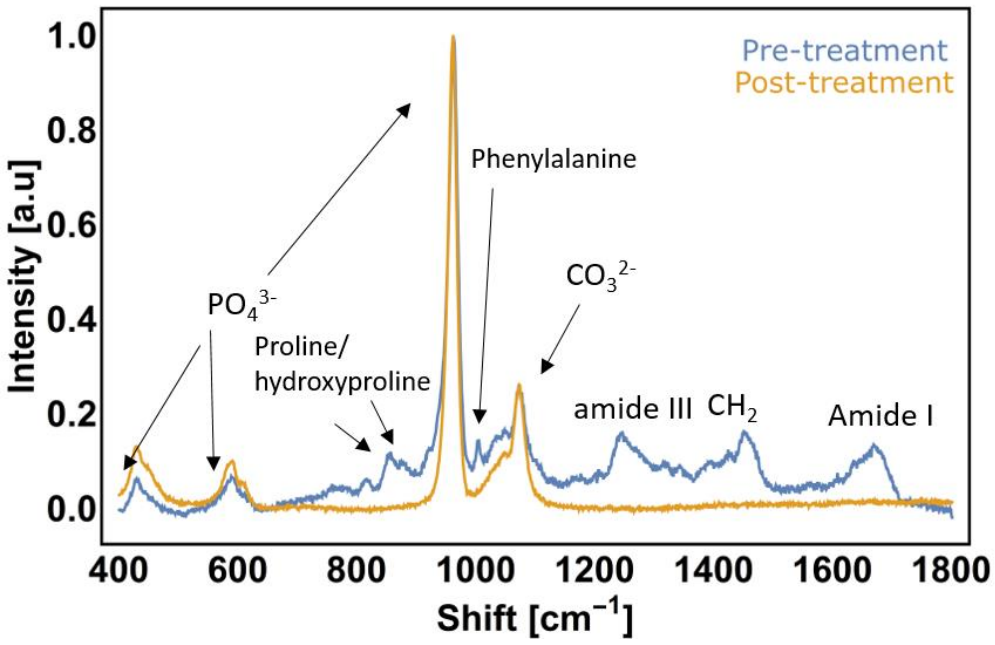

Figure S4. Raman spectra before and after NaOCl deproteination of bone showing disappearance of all protein peaks after the treatment.

Appendix 1: Re-adjusted (adj) volume fractions to account for ϕ_{flaws}^{EFM} . These are the values reported in Supplementary Table 1 without the "adj" for simplicity.

$$\phi_{Min,adj} = \phi_{Min}\ (\phi_{IF}^{Min} + \phi_{EF}^{Min}(1 - \phi_{flaws}^{EFM}\ )$$

$$\phi_{EF}^{Min,adj} = \frac{\phi_{EF}^{Min}\left(1 - \phi_{flaws}^{EFM}\right)}{\phi_{Min}^{adj}}$$

$$\phi_{IF}^{Min,adj} = 1 - \phi_{EF}^{Min,adj}$$

$$\phi_{Min,adj}^{EFM} = \phi_{Min}^{EFM}(1 - \phi_{flaws}^{EFM})$$

$$\phi_{NCP,adj}^{EFM} = 1 - \phi_{Min,adj}^{EFM} - \phi_{flaws}^{EFM}$$

$$\phi_{NCP,adj} = \phi_{NCP,adj}^{EFM}\ \phi_{EFM}$$

Appendix 2: Matlab code for analyzing pores in SEM images

```
%% Pore Thresholding and Analysis
% This script uses binary thresholding to count and measure the
% the pores in the SEM tomographs of bone. As written it takes as
% input SEM jpeg images but this can be modified.
%
%

%% Import names of jpegs
% the source directory can be modified
imageNames = dir(fullfile('jpegs','originals','*.jpg'));
imageNames = {imageNames.name}';


%% Crop and threshold SEM images to outline pores

% set cropping rectangle
mCrop = [0 100 1200 800];

% loop runs through each image
for i=1:length(imageNames)
    %% Threshold and identify pores
    %read and crop SEM jpeg
    rgb1 = imread(fullfile('jpegs','originals',imageNames{i}));
    rgb2 = imcrop(rgb1,mCrop);

    %convert jpeg to grayscale and saturate the top and bottom 1percent
    gray1 = rgb2gray(rgb2);
    gray2 = imadjust(gray1);

    % convert gray scale to binary and complement the image
    bwimage = im2bw(gray2,.25);
    bwimage = imcomplement(bwimage);

    % size threshold pores under 20pixels to remove noise
    bwimage = bwareaopen(bwimage,20);

    % use small cylindrical structuring close off perimeters of pores
    se = strel('disk', 7); %# structuring element
    closeBW = imclose(bwimage,se);
    closeBW2 = bwperim(closeBW,8);
    closeBW2 = imcomplement(closeBW2);

    %% Overlay original image with red outlines of the detected pores
    %map binary to rgb
    [x,map2]= gray2ind(closeBW2,2);
    % colormap to map black to red and white to white
    map = [1 0 0;1 1 1];
    %convert binary to RGB and map it as described above
    bwRGB = ind2rgb(x,map);
    mask = cast(bwRGB, class(rgb2));
    imgMasked = rgb2 .*mask;
```

```
    %% Output resulting images to desired folders
    % output binary images
    % output cropped original rgb
    % output red outline overlaid images to create supplementary video


if i<10
    imwrite(closeBW2,fullfile('jpegs','binary',['disorderedBW_0' num2str(i)
'.jpg']));
    imwrite(rgb2,fullfile('jpegs','binary',['disorderedCrop_0' num2str(i)
'.jpg']));
else
      imwrite(closeBW2,fullfile('jpegs','binary',['disorderedBW_' num2str(i)
'.jpg']));
    imwrite(rgb2,fullfile('jpegs','binary',['disorderedCrop_' num2str(i)
'.jpg']));
end


end

%% Measure Properties of holes
% This section can be run as a separate script. We import the binary (BW)
% images from the previous section/script and use the regionprops function
% to analyze the properties of the pores.


% set scale pixel to micron conversion scale
% manually measured from any one of the original SEM images via imageJ
oneMicron = 440; % 1um = 440 pixels

% import image names
imageNames = dir(fullfile('jpegs','binary','disorderedBW*'));
imageNames = {imageNames.name}';
l = length(imageNames)

% assign zeroed arrays for values of interest
fractions = zeros(1,l);
radii = zeros(1,l);
sigRadii = zeros(1,l);
totArea = 801*1200;

% loop runs through each binary image, collects radii and volume fractions
% of the regions
for j=1:l
    %import image
    img = imread(fullfile('jpegs','binary',imageNames{j}));

    %convert and complement and and fill in pores as they are currently
    % only identified by their perimiters
    img = im2bw(img,graythresh(img));
    img = imcomplement(img);
    imgBW = imfill(img, 'holes');
```

```
    % collect pore information
    stats = regionprops(imgBW,{'Area','EquivDiameter'});
    filled = sum([stats(:).Area]);
    fractions(j) = filled/totArea;
    radii(j) = mean([stats(:).EquivDiameter])/2;
    currentRadii = [stats(:).EquivDiameter]/2;

    %append pore radii to array of radii
    if j == 1
        allRadii = currentRadii;
    else
        allRadii = [allRadii currentRadii];
    end
end

% calculate mean and std of radii and volume fraction of pores
meanRadii = mean(allRadii(:)/oneMicron)
sigRadii = std(allRadii(:)/oneMicron)
meanFractions = mean(fractions(:))


%% End of script
```

References

1. Mahamid, J. *et al.* Mapping amorphous calcium phosphate transformation into crystalline mineral from the cell to the bone in zebrafish fin rays. *Proc. Natl. Acad. Sci. U. S. A.* **107,** 6316–6321 (2010).
2. Daniel, M. I. & Ishai, O. *Engineering Mechanics of Composite Materials*. (Oxfored University Press, Inc., 2006).
3. Jäger, I. & Fratzl, P. Mineralized collagen fibrils: a mechanical model with a staggered arrangement of mineral particles. *Biophys. J.* **79,** 1737–1746 (2000).
4. Nudelman, F. *et al.* The role of collagen in bone apatite formation in the presence of hydroxyapatite nucleation inhibitors. *Nat. Mater.* **9,** 1004–1009 (2010).
5. Hassenkam, T. *et al.* High-resolution AFM imaging of intact and fractured trabecular bone. *Bone* **35,** 4–10 (2004).
6. Schwiedrzik, J. *et al.* In situ micropillar compression reveals superior strength and ductility but an absence of damage in lamellar bone. *Nat. Mater.* **13,** 1–8 (2014).
7. Thurner, P. J. *et al.* High-speed photography of compressed human trabecular bone correlates whitening to microscopic damage. *Eng. Fract. Mech.* **74,** 1928–1941 (2007).
8. Alexander, B. *et al.* The nanometre-scale physiology of bone: steric modelling and scanning transmission electron microscopy of collagen-mineral structure. *J. R. Soc. Interface* **9,** 1774–1786 (2012).
9. Lees, S., Prostak, K. S., Ingle, V. K. & KjollerK. The Loci of Mineral in Turkey Leg Tendon As Seen By Atomic Force Microscope and Electron Microscopy. *Calcif. Tissue Int.* 180–189 (1994).
10. Nikolov, S. & Raabe, D. Hierarchical Modeling of the Elastic Properties of Bone at Submicron Scales : The Role of Extrafibrillar Mineralization. *Biophys. J.* **94,** 4220–4232 (2008).
11. Nair, A. K., Gautieri, A., Chang, S.-W. & Buehler, M. J. Molecular mechanics of mineralized collagen fibrils in bone. *Nat. Commun.* **4,** 1724 (2013).
12. Hamed, E., Jasiuk, I., Yoo, a., Lee, Y. & Liszka, T. Multi-scale modelling of elastic moduli of trabecular bone. *J. R. Soc. Interface* **9,** 1654–1673 (2012).
13. Bonar, L. C., Lees, S. & Mook, H. A. Neutron diffraction studies of collagen in fully mineralized bone. *J. Mol. Biol.* **181,** 265–270 (1985).
14. Li, S. X., Zhao, J., Lu, P. & Xie, Y. Maximum packing densities of basic 3D objects. *Chinese Sci. Bull.* **55,** 114–119 (2010).
15. Timoshanko, S. P. & Goodier, J. N. *Theory of Elasticity*. (McGraw-Hill Book Company, 1970).
16. Turner, C. H., Rho, J., Takano, Y., Tsui, T. Y. & Pharr, G. M. The elastic properties of trabecular and cortical bone tissues are similar: Results from two microscopic measurement techniques. *J. Biomech.* **32,** 437–441 (1999).
17. Inglis, C. E. Stresses in a plate due to the presnce of cracks and sharp corners. *Trans. I.N.A.* **XLIV,** 15 (1913).
18. Parthasarathy, T. a., Rao, S. I., Dimiduk, D. M., Uchic, M. D. & Trinkle, D. R. Contribution to size effect of yield strength from the stochastics of dislocation source lengths in finite samples. *Scr. Mater.* **56,** 313–316 (2007).